Journal of Sound and Vibration 618 (2025) 119322

Contents lists available at ScienceDirect

Journal of Sound and Vibration

journal homepage: www.elsevier.com/locate/jsvi

Sensitivity and optimisation of the acoustic response of short circular holes with turbulent bias flow

Juan Guzmán-Iñigo [a,b,*], Dania Ahmed [b,c], Aimee S. Morgans [b]

[a] Department of Engineering, City St George's, University of London, London, UK
[b] Department of Mechanical Engineering, Imperial College London, London, UK
[c] Department of Mechanical and Aerospace Engineering, University of Manchester, Manchester, UK

ARTICLE INFO

Keywords:
Perforations
Acoustic damping
Optimisation
Bias flow

ABSTRACT

Short circular holes with turbulent bias flows passing through them can absorb or generate acoustic energy. This property is relevant for many industrial applications, such as liners and injectors. A recent study suggested that the acoustic response of such perforations could be strongly sensitive to small modifications of the geometries of their lips. In this work, we study this sensitivity and exploit it to design holes with optimal acoustic properties. To this end, we use a numerical approach based on a two-step method, where a steady mean flow is first calculated as the solution of the incompressible RANS equations. Small-amplitude acoustic perturbations are then superimposed on this mean flow, and their dynamics are obtained by solving the linearised Navier–Stokes equations. To validate the approach, the results are compared with experiments for a hole with sharp edges, finding an excellent agreement. Subsequently, we simulate four holes with modified corners consisting in chamfers or circular fillets either of the upstream or downstream corners. The acoustic absorption is found to be strongly sensitive to all modifications with the upstream chamfer presenting the strongest variations. Finally, we combine the simulations with a Bayesian optimisation algorithm to obtain the size of the upstream chamfer that maximises the acoustic absorption. The optimised hole goes from exhibiting strong whistling to one which strongly damps acoustic energy.

1. Introduction

Circular holes with a turbulent bias flow passing through them can absorb or generate acoustic energy. This property is relevant for many industrial applications, such as propellant injectors in rocket engines [1–3] or acoustic liners [4–6] and Helmholtz resonators [7,8] in gas turbines. For most of these applications, it is desirable to maximise the acoustic energy absorbed by the holes.

The topology of the flow passing through this type of holes is determined by the ratio between the hole's length (thickness) to its diameter [9]. Regardless of this ratio, the flow separates at the upstream rims of the hole resulting in a low-speed recirculation region close to the internal walls and a high-speed central jet. If the length of the hole is insufficient, the flow remains separated along its whole length. This type of holes are called short (thin) holes. On the other hand, if the hole is long enough, the boundary layer is reenergised by turbulence and the flow reattaches inside it. This flow topology corresponds to long (thick) holes. The present work focus on short circular holes.

* Corresponding author at: Department of Engineering, City St George's, University of London, London, UK.
E-mail address: juan.guzman@city.ac.uk (J. Guzmán-Iñigo).

https://doi.org/10.1016/j.jsv.2025.119322
Received 29 November 2024; Received in revised form 2 July 2025; Accepted 2 July 2025
Available online 14 July 2025

The acoustics of short circular holes with turbulent bias flow have been widely investigated experimentally [10–12], theoretically [13–16] and numerically [17–21]. At low frequencies, acoustic absorption occurs as a result of the transfer of acoustic energy to vortical energy (in the form of unsteady vorticity). When incident acoustic waves interact with the shear layers at the rims of a hole, unsteady vorticity is shed at the lips. At high Reynolds numbers, this unsteady vorticity is convected through the hole by the mean flow and eventually dissipated by turbulence far downstream. Theoretical models of the acoustic response of holes usually assume that the vorticity shed at the hole inlet edge is convected downstream by the mean flow to form a thin vortex sheet within the mean shear layer [13].

Recent semi-analytical models [15,16] which account for the vortex–sound interactions both after and within the short hole revealed the importance of accurately capturing the path of the shed vorticity (or the vortex sheet shape). This path is, in turn, strongly sensitive to small modifications to the shape of the lips of the perforation. Combining both effects, Guzman-Inigo et al. [22] found that the acoustic response of the perforations is indeed very sensitive to small modifications of the geometry. This sensitivity — already well known for the mean flow properties [23–25] (pressure loss across the hole/discharge coefficient) – is significantly more pronounced for the acoustics.

In this work, we explore for the first time the sensitivity of the acoustic response of short circular holes with bias flow to small modifications of their corner rims using numerical simulations, extending previous studies [22] based on semi-analytical models. The numerical approach is a two-step method [26,27] revolving around a frequency-domain implementation of the linearised Navier–Stokes equations (LNSE) with eddy viscosity. This methodology is highly efficient and is combined in a second step with a Bayesian optimisation algorithm to find the geometry that maximises the acoustic energy absorbed by the perforations [28]. Alternatively, adjoint-based shape optimisation [29–32] or level-set topological optimisation [33] could be employed.

The effect of the shape on the acoustics of holes has been investigated by many authors. For example, circular holes without mean flow have been explored experimentally and numerically by [34,35], respectively. As for holes in the presence of bias flow, as considered in this publication, Ji et al. [36,37] determined – using numerical simulations and experiments – that large modifications to the edges of such holes (symmetric chamfers and fillets) strongly modify their acoustic response. Similarly, Testud et al. [10] performed experiments of a hole with relatively large chamfered edges (either upstream or downstream) and found that the whistling potentiality was suppressed in the presence of a downstream chamfer, but not with an upstream one. Finally, Zhao et al. [38] carried out experiments of holes with different cross-section shapes (not circular) with similar results.

All the aforementioned studies considered large geometrical modifications of the holes. In this work, instead, we focus on the sensitivity to very small modifications. The contributions of the present article are twofold. First, we confirm that short circular holes with a bias flow passing through them are indeed strongly sensitive to small modifications of both the upstream or downstream edges, being the former particularly strong. This highlights the need to account for this sensitivity when modelling/manufacturing/designing acoustic systems containing them. Second, we extend previous methodologies to design optimal edges (in the acoustic sense) for laminar flows [28] to the turbulent regime.

This article is structured as follows. The configuration and the numerical approach are presented in Section 2. The numerical results for a straight hole (sharp edges) are compared in Section 3 with experimental measurements to validate the approach. In Section 4, the sensitivity of the acoustic response to small modifications (chamfers/fillets) of the hole corners is investigated. In Section 5, the numerical solver is combined with an optimisation algorithm to obtain the size of the upstream chamfer that maximises acoustic absorption. A summary and conclusions are given in Section 6.

2. Problem formulation

2.1. Configuration

We consider a circular hole of radius R_h and area A_h perforated on a flat plate of thickness L_h that separates two concentric, circular ducts as sketched in Fig. 1. A subsonic flow in the streamwise direction is imposed on the left-hand side of the domain. The left-hand- and right-hand-side ducts are denoted, respectively, upstream and downstream ducts and all the variables defined in them are denoted by the subscripts $(\cdot)_u$ and $(\cdot)_d$, respectively. The variables defined inside the hole are denoted by the subscript $(\cdot)_h$.

The flow at the inlet consists of a uniform component of velocity $\bar{\mathbf{u}}_u = \bar{u}_u \mathbf{e}_x$ (with $\mathbf{e}_x$ the unit vector in the axial direction) and speed of sound $\bar{c}_u$. The mean flow velocity can be normalised by the speed of sound to define the inlet Mach number $M_u = \bar{u}_u/\bar{c}_u$. Small-amplitude incoming acoustic waves are superimposed on this mean flow. The flow variables can be decomposed into a steady mean, denoted by $\bar{(\cdot)}$, and a perturbation component, denoted by $\tilde{(\cdot)}$. The perturbation component is small and, thus, the equations governing its evolution can be linearised around the mean flow allowing us to use the harmonic ansatz

$$\tilde{(\cdot)} = \hat{(\cdot)} \exp(\mathrm{i}\omega t), \tag{1}$$

where $\omega = 2\pi f$ is the angular frequency, t the time, and i the imaginary unit. The frequency of the perturbations, f, can be non-dimensionalised to form a Strouhal number as follows:

$$St = \frac{f L_h}{\bar{u}_h}, \tag{2}$$

with $\bar{u}_h$ denoting the bulk velocity in the hole and L_h the thickness of the plate.

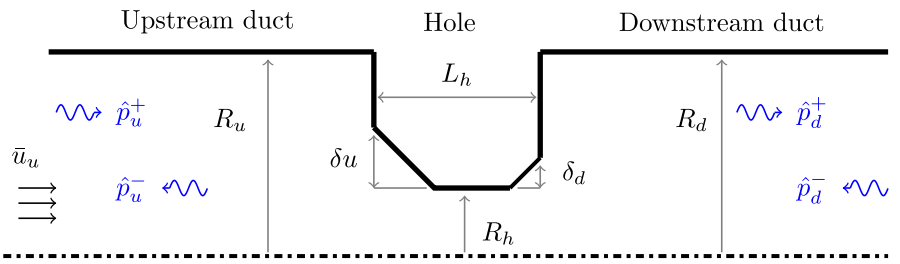

Fig. 1. Schematic of the configuration. The dash-dotted line indicates the axis of revolution. Chamfers defined by 45° angles or circular fillets are applied to the corners of the hole. The characteristic size of the modifications is denoted δ_u and δ_d for the upstream and downstream corners, respectively.

Far from the area expansion, the acoustic field is composed of plane waves (see Fig. 1) propagating in the same and opposite direction to the mean flow and denoted by $\hat{(\cdot)}^+$ and $\hat{(\cdot)}^-$, respectively. The perturbation pressure and axial velocity can be written in terms of the plane waves as $\hat{p} = \hat{p}^+ + \hat{p}^-$ and $\hat{u} = \left(\hat{p}^+ - \hat{p}^-\right)/(\bar{\rho}\bar{c})$, respectively, where $\bar{\rho}$ denotes the mean density.

The working fluid is taken to be a Newtonian, compressible, calorically perfect gas. The flow is determined by two non-dimensional parameters: the Reynolds number, $Re = (\bar{\rho}_h \bar{u}_h R_h)/\mu$, and the bulk Mach number at the perforation, $M_h = \bar{u}_h/\bar{c}_h$. μ is the dynamic viscosity. Heat transfer and body forces are neglected. The Mach number throughout the domain is assumed to be small, i.e. $M_h \ll 1$, and the Reynolds number is high enough for turbulence to occur.

2.2. Numerical implementation

In this section, we present the numerical methodology employed to characterise the acoustic response of the perforations. We solve the governing equations for the mean and perturbation parts separately.

A triple decomposition [39] is introduced in the governing equations following [26,27]. Because of the low-Mach numbers of interest, the mean flow is assumed to be incompressible and is governed by the incompressible Reynolds-Averaged Navier–Stokes (RANS) equations that are solved using the open-source finite volume solver OpenFOAM (version 4.1) [40]. A steady state solution is obtained using the SIMPLE algorithm. The eddy viscosity, μ_t, is determined using the k-omega-SST model [41].

The governing equations for the perturbation are subsequently linearised around this mean flow to obtain,

$$\frac{\partial \tilde{\rho}}{\partial t} + \nabla \cdot (\bar{\rho}\tilde{\mathbf{u}} + \tilde{\rho}\bar{\mathbf{u}}) = 0, \tag{3a}$$

$$\frac{\partial \bar{\rho}\tilde{\mathbf{u}}}{\partial t} + (\bar{\rho}\tilde{\mathbf{u}} + \tilde{\rho}\bar{\mathbf{u}}) \cdot \nabla\bar{\mathbf{u}} + \nabla \cdot (\bar{\rho}\bar{\mathbf{u}} \otimes \tilde{\mathbf{u}}) = -\nabla\tilde{p} + \nabla \cdot \underline{\underline{\tilde{\boldsymbol{\tau}}}}^{\mathrm{tot}}, \tag{3b}$$

where the fluctuation total stress tensor is given by

$$\underline{\underline{\tilde{\boldsymbol{\tau}}}}^{\mathrm{tot}} = \underline{\underline{\tilde{\boldsymbol{\tau}}}} - \left(\left\langle \rho\mathbf{u}' \otimes \mathbf{u}' \right\rangle - \overline{\rho\mathbf{u}' \otimes \mathbf{u}'} \right), \tag{4a}$$

with

$$\underline{\underline{\tilde{\boldsymbol{\tau}}}} = \mu \left[\left(\nabla\tilde{\mathbf{u}} + \nabla\tilde{\mathbf{u}}^{\top} \right) - \frac{2}{3} (\nabla \cdot \tilde{\mathbf{u}}) \underline{\underline{\mathrm{I}}} \right]. \tag{4b}$$

$\overline{(\cdot)}$ is the time-average operator, $\langle\cdot\rangle$ the phase-average operator, and $\underline{\underline{\mathrm{I}}}$ the identity tensor. $(\cdot)'$ denotes turbulent fluctuations. Following [39], a closure model for the fluctuations of the Reynolds stress tensor is proposed. This closure assumes that the fluctuations are proportional to the fluctuations of the strain-rate tensor as

$$-\left(\left\langle \rho\mathbf{u}' \otimes \mathbf{u}' \right\rangle - \overline{\rho\mathbf{u}' \otimes \mathbf{u}'} \right) = \mu_t \left[\left(\nabla\tilde{\mathbf{u}} + \nabla\tilde{\mathbf{u}}^{\top} \right) - \frac{2}{3} (\nabla \cdot \tilde{\mathbf{u}}) \underline{\underline{\mathrm{I}}} \right]. \tag{5}$$

Additionally, we assume that the turbulence is not affected by the acoustic fluctuations which allows the eddy viscosity to be considered "frozen" and equal to the value obtained for the mean flow from the RANS simulations.

If we further assume homentropicity, a relation between density and pressure can be obtained by linearising the Gibbs relation. The resulting expression is then integrated from a reference state, to obtain

$$\tilde{p} = \bar{c}^2 \tilde{\rho}. \tag{6}$$

This relation has been widely used in similar numerical implementations for low-Mach-number configurations [26,27,42–44].

The linearised equations are then recast in the frequency domain and solved using a finite element method stabilised with a least-squares formulation [45]. The equations are implemented in the open-source computing framework FEniCS [46,47]. After discretisation, the resulting linear system is inverted using the sparse direct solver MUMPS [48,49]. The numerical implementation has been validated with several canonical test cases [50], including an isentropic nozzle and the acoustic scattering of an area expansion.

At the inlet and outlet of the domain, non-reflecting boundary conditions are imposed. The implementation of the boundary conditions is based on the splitting of the flux vector defined at the boundaries (that appears naturally in the formulation after integration by parts) into incoming and outgoing waves [9] in a similar way as that of the characteristics method [51]. This method allows incoming acoustic waves to be easily imposed at both boundaries while assuring non-reflectivity of the outgoing waves. The resulting acoustic field is subsequently post-processed using the multi-microphone method [52,53] to separate the two components of the acoustic plane waves.

2.3. Flow characterisation

The mean flow will be characterised using the discharge coefficient, C_d, defined as the ratio of the actual mass flow rate at the hole to that of an ideal nozzle:

$$C_d = \bar{u}_h / \bar{u}_{\text{ideal}}, \tag{7}$$

where

$$\bar{u}_{\text{ideal}} = \sqrt{2\Delta\bar{p}/\bar{\rho}} / \sqrt{1 - \left(R_h/R_u\right)^4}, \tag{8}$$

and $\Delta\bar{p}$ the mean pressure difference across the hole.

The acoustic response of the perforations will be characterised using both the impedance and the scattering matrix [54]. The impedance is given here in its normalised form,

$$Z_h = \frac{1}{\bar{\rho}\bar{c}} \frac{\Delta\hat{p}_h}{\hat{u}_h} = Z_R + \mathrm{i} Z_I, \tag{9}$$

where $\Delta\hat{p}_h$ is the difference in acoustic pressure across the orifice and $\hat{u}_h$ is the axial acoustic velocity at the inlet of the orifice. Here, $\hat{u}_h$ is obtained indirectly from the acoustic velocity of the plane waves in the upstream duct using the continuity equation at the perforation's inlet, i.e. $\hat{u}_u A_u = \hat{u}_h A_h$. Z_R represents the in-phase component, known as resistance, and Z_I is the out-of-phase component, known as reactance.

The quasi-steady resistance, $Z_{R,\text{qs}}$, is related to the discharge coefficient as [20],

$$Z_{R,\text{qs}} = \frac{1}{\bar{\rho}\bar{c}} \frac{\partial\Delta\bar{p}}{\partial\bar{u}_h} = \frac{M_h}{C_d^2} \left(1 - \left(R_h/R_u\right)^4\right). \tag{10}$$

The scattering matrix [54] summarises the relation between acoustic waves:

$$\begin{pmatrix} \hat{p}_d^+ \\ \hat{p}_u^- \end{pmatrix} = \begin{pmatrix} T^+ & R^- \\ R^+ & T^- \end{pmatrix} \begin{pmatrix} \hat{p}_u^+ \\ \hat{p}_d^- \end{pmatrix}. \tag{11}$$

Finally, we analyse the energy balance of the perforation using the absorption coefficient, Δ, of the domain defined as [55–57]

$$\Delta = 1 - \frac{|W_u^-| + |W_d^+|}{|W_u^+| + |W_d^-|}, \tag{12}$$

where $W_j^{\pm}$ (for j = u, d) is the time-averaged surface-averaged acoustic energy flux [58] associated with the wave propagating in the positive/negative direction and given by $W_j^+ = \left(1 + M_j\right)^2 |\hat{p}_j^+|^2 A_j/(\bar{\rho}_j \bar{c}_j)$ and $W_j^- = \left(1 - M_j\right)^2 |\hat{p}_j^-|^2 A_j/(\bar{\rho}_j \bar{c}_j)$. The acoustic absorption coefficient compares the average amount of acoustic energy entering and leaving the domain. If there is no outgoing acoustic energy on average then $\Delta = 1$. The relative amount of outgoing acoustic energy then increases as the acoustic absorption coefficient decreases, until it becomes equal to the amount of incoming acoustic energy for $\Delta = 0$. Finally, there is more acoustic energy leaving the control volume than entering it on average for $\Delta < 0$.

3. Validation: Straight hole

To assess the suitability of the numerical approach, we compare the numerical results with the experimental measurements of Lacombe et al. [10,18]. The operating condition considered here corresponds to the operating condition number 1 as defined in [18]. The flow is determined by the parameters $Re = 20{,}000$ and $M_h = 0.104$. The geometry is defined by $R_u/R_h = R_d/R_h = 2$ and $L_h/R_h = 2/3$.

3.1. Mean flow

We now present the details of the mean flow computations. Exploiting the rotational symmetry of the problem, the structured mean flow mesh is a 5° wedge composed of hexahedral cells with a row of prismatic cells around the axis of revolution. This mesh extends only one layer in the circumferential direction with boundary conditions in the two bounding planes that ensure axisymmetry of the flow variables. The walls of the ducts and the hole are treated with a non-slip boundary condition $\bar{\mathbf{u}} = 0$. At the walls, the mesh resolves the boundary layer with a dimensionless wall distance of $y+ < 1$ to avoid the use of wall functions for the turbulence modelling. A fully-developed turbulent flow profile is set at the inlet to yield a mean velocity of $\bar{u}_h = 1$ inside the hole. This profile was obtained from a separate simulation of a long duct. The velocity, turbulent kinetic energy and specific rate

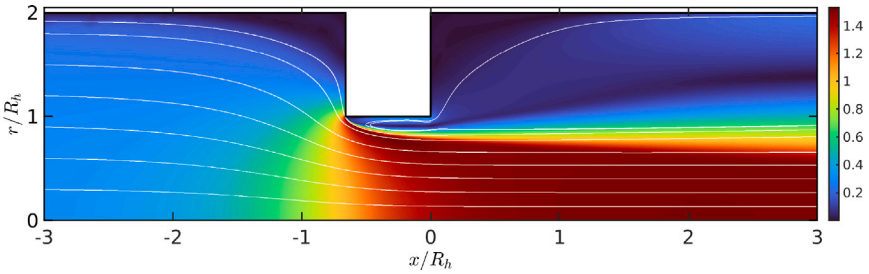

Fig. 2. Mean flow velocity magnitude, $|\bar{\mathbf{u}}|/\bar{u}_h$, obtained for a straight hole.

of turbulent dissipation (omega) are imposed. Zero gradient is set for the pressure at the inlet. The flow leaves the computational domain at prescribed zero relative pressure and the gradients of velocity, specific dissipation rate of turbulent kinetic energy and turbulent kinetic energy are set to zero at the outlet. The lengths of the pipes upstream and downstream are $110R_h$ each. The mesh is composed of 101,079 cells.

Fig. 2 shows the mean flow obtained using this approach. The flow cannot follow the sharp geometry of the hole at the inlet and separates creating a low-speed recirculation region adjacent to the wall. A jet is created in the central zone of the hole. A shear layer separates these regions. The thickness of the recirculation zone rapidly increases downstream of the inlet contraction. The velocity of the jet increases due to the reduction of the effective flow area produced by the presence of the separation. This increment of velocity, however, comes at the expense of a pressure drop. Downstream of the perforation the flow is largely detached.

3.2. Acoustic response

We now turn our attention to the acoustic fluctuations. As for the mean flow computations, the rotational symmetry of the problem is exploited in the acoustic simulations. The governing equations are formulated in cylindrical coordinates and an unstructured two-dimensional mesh consisting of triangular elements is used. Anechoic acoustic boundary conditions based on a flux vector splitting approach are set at the domain inlet and outlet. The walls containing the hole are treated with a non-slip boundary condition $\hat{\mathbf{u}} = 0$. For the acoustics, the walls of the upstream and downstream ducts are modelled using a slip boundary condition $\hat{\mathbf{u}} \cdot \mathbf{n} = 0$ to reduce the computational cost associated with solving the acoustic boundary layer (with $\mathbf{n}$ denoting the unitary vector normal to the wall). Comparative studies between simulations using acoustic no-slip and slip boundary conditions at the downstream duct wall showed only a minor influence on the results. Additionally, Kierkegaard et al. [59] reported that a high resolution of the acoustic boundary layer is not necessary to obtain reliable results. Two sets of simulations were performed to obtain the scattering matrix: forcing upstream and downstream separately. Figs. 3 and 4 show the results obtained for the scattering matrix. As observed, the agreement between the numerical results and the experimental data is excellent. This agreement is almost as good as obtained with high-fidelity LES simulations [18]. This simulation validates the numerical method selected to characterise the acoustic response of the perforations.

4. Sensitivity of the acoustic response to edge modifications

In this section, we compare the results obtained for a straight hole with holes with 45° chamfered edges and circular fillets. The size of the chamfers and fillets are defined by the characteristic length δ representing the projected chamfer length for the chamfers and the fillet radius for the fillets (Fig. 1). We consider modifications either of the upstream or downstream edges (with sizes denoted δ_u and δ_d, respectively).

4.1. Mean flow sensitivity

The four modifications are depicted in Fig. 5 for $\delta/R_h = 5\%$. We observe that the presence of the chamfers/fillets upstream helps the flow pass the inlet edge and a much thinner recirculation zone is obtained than for the straight cases. As a consequence, the effective area available for the central flow is larger and, thus, the speed of the central jet is reduced. The modifications downstream, on the other hand, only modify the flow locally close to the corner and, thus, the thickness of the recirculation zone and speed of the jet remain apparently unmodified. The effect of the modifications can be further quantified by computing the discharge coefficient, C_d, of the holes.

Table 1 presents the discharge coefficient for six cases: (i) a straight hole, holes with upstream-chamfered edges defined by (ii) $\delta_u/R_h = 2.5\%$ and (iii) $\delta_u/R_h = 5\%$, (iv) a hole with a chamfer at the downstream edge $\delta_d/R_h = 5\%$, and fillets at the (v) upstream and (vi) downstream edges both of size $\delta/R_h = 5\%$. The mean pressure drop was measured between $x = -5$ and the backplate at

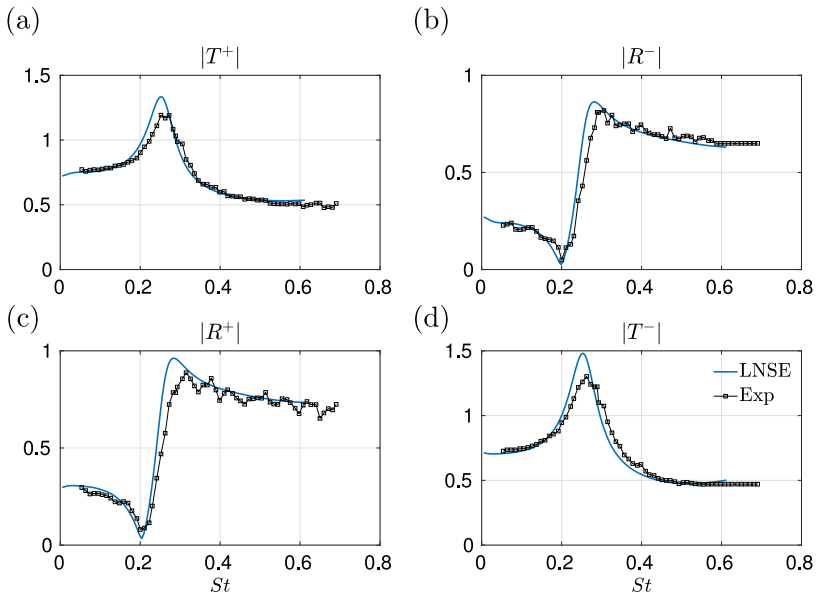

Fig. 3. Absolute value of the scattering coefficients: (a) $|T^+|$, (b) $|R^-|$, (c) $|R^+|$, and (d) $|T^-|$. (Black solid line with squares) experimental results [18] and (blue solid line) numerical results.

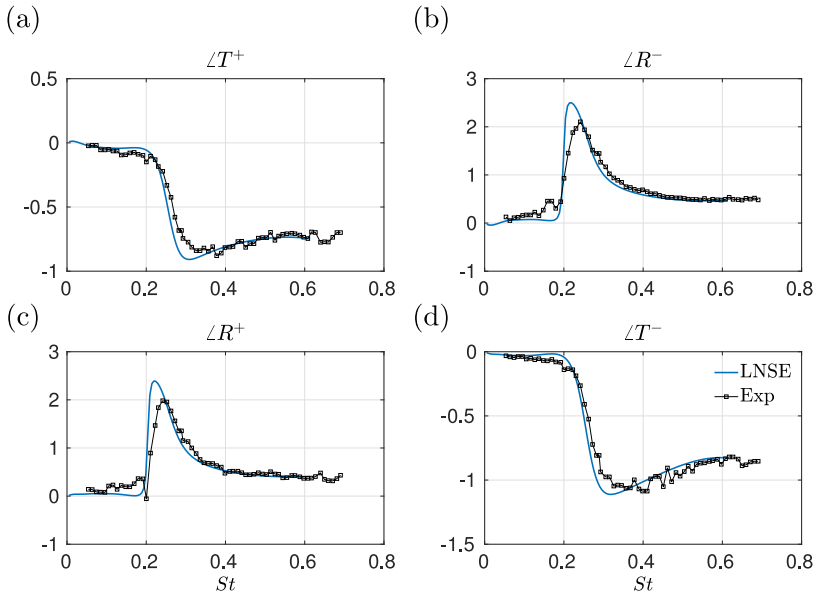

Fig. 4. Phase of the scattering coefficients: (a) $\angle T^+$, (b) $\angle R^-$, (c) $\angle R^+$, and (d) $\angle T^-$. (Black solid line with squares) experimental results [18] and (blue solid line) numerical results.

$x = 0$. We observe that the discharge coefficient of the straight and the downstream-chamfered/rounded holes is virtually identical. In contrast, when the modifications are at the upstream edge, the discharge coefficient is strongly increased with increasing values of δ_u (larger modifications). This can be attributed to the reduced thickness of the recirculation zone near the wall, resulting from the upstream chamfers or fillets (Fig. 5). In addition, note that upstream chamfers have a substantially stronger effect on the flow

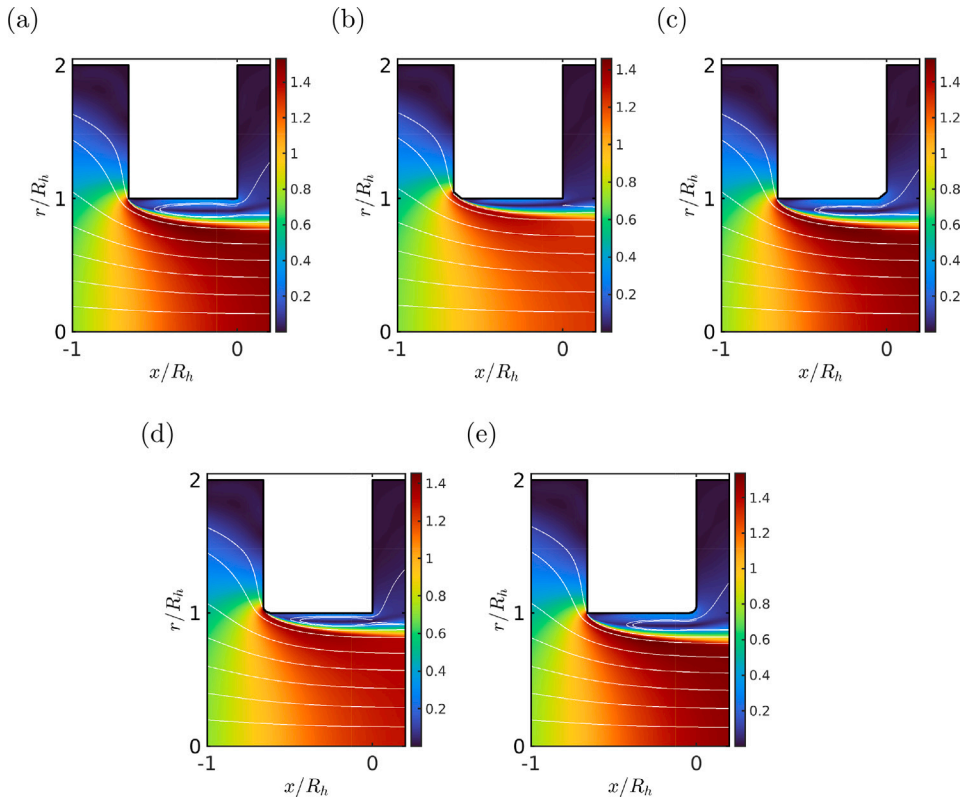

Fig. 5. Mean flow velocity magnitude, $|\bar{\mathbf{u}}|/\bar{u}_h$, obtained for: (a) a straight hole, holes with chamfered (b) upstream and (c) downstream edges, and holes with fillets at the (d) upstream and (e) downstream edges. $\delta/R_h = 5\%$.

Table 1
Discharge coefficient, C_d, and quasi-steady resistance, $Z_{R,\mathrm{qs}}$, for the different perforations.

		Straight	
C_d		0.65	
$Z_{R,\mathrm{qs}}$		0.23	
		Chamfer	
	Upstream 2.5%	Upstream 5%	Downstream 5%
C_d	0.72	0.78	0.65
$Z_{R,\mathrm{qs}}$	0.19	0.16	0.23
		Fillet	
		Upstream 5%	Downstream 5%
C_d		0.74	0.64
$Z_{R,\mathrm{qs}}$		0.18	0.24

than upstream fillets. This may occur because, for the chamfers, the local velocity at the point of separation forms a shallower angle compared to that of the fillet, leading to a thinner recirculation region.

The values of the quasi-steady resistance are also presented in Table 1. Those values indicate that the resistance of the perforation at very low frequencies is expected to significantly decrease with upstream small modifications [20] and remain virtually unchanged with downstream ones.

4.2. Sensitivity of the acoustic response

Fig. 6 shows the acoustic impedance of the straight hole compared to holes with chamfered upstream edges of sizes $\delta_u/R_h = 2.5\%$ and $\delta_u/R_h = 5.0\%$. We observe that both the resistance and reactance are dramatically affected by the two chamfers. In Fig. 7(a)

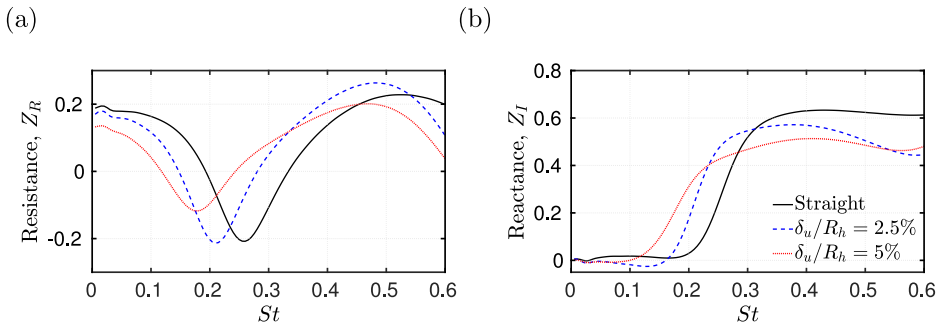

Fig. 6. Normalised impedance, $Z = Z_R + \mathrm{i}Z_I$, for holes with chamfered upstream edges. (a) Resistance, Z_R, and (b) reactance, Z_I.

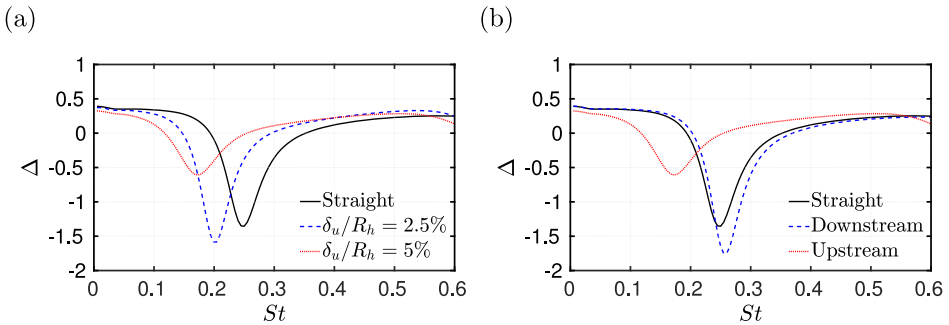

Fig. 7. Acoustic absorption, Δ, for holes forced by incoming acoustic waves at the inlet. (a) Chamfers at the upstream edge. (b) Chamfers either at the upstream or downstream edges of size $\delta/R_h = 5\%$.

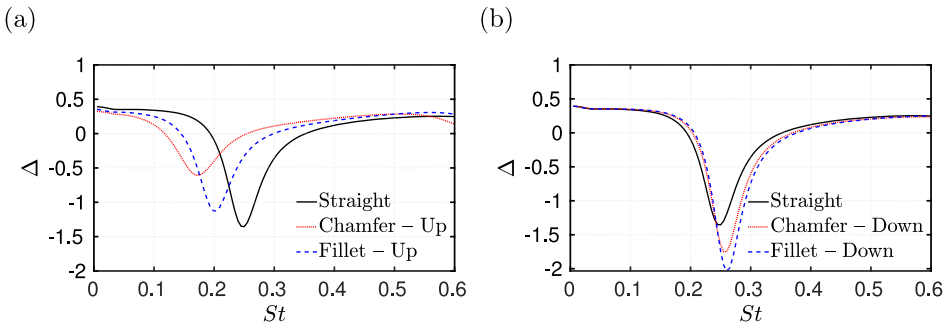

Fig. 8. Acoustic absorption, Δ, for holes forced by incoming acoustic waves at the inlet. (a) Upstream-edge modifications. (b) Downstream-edge modifications. The sizes of the four modifications are $\delta/R_h = 5\%$.

the absorption coefficient obtained for these three geometries forced by upstream-incoming acoustic waves is depicted. The straight hole generates acoustic energy (whistles) at frequencies $0.2 < St < 0.35$. This whistling region is displaced to lower frequencies with increasing upstream chamfer sizes. This can be explained by the lower bulk velocity in the hole and, therefore, the lower convective velocity of the vorticity fluctuations. The peak of energy generation is also greatly affected, going from generating 134% more acoustic energy than incident upon it at the peak to 160% and 60% for the chamfers of size $\delta_u/R_h = 2.5\%$ and $\delta_u/R_h = 5.0\%$, respectively. Contrarily, Fig. 7(b) shows that the chamfer at the downstream edge only mildly modifies the acoustic absorption: the peak is displaced to slightly higher frequencies and its magnitude increased from $\Delta = -1.35$ to $\Delta = -1.75$.

Fig. 8 compares the absorption coefficient obtained for chamfers and fillets of the same size ($\delta/R_h = 5\%$). The same trends are obtained for the two types of modifications introduced either upstream or downstream. The results for the upstream, however, show that the acoustic absorption is substantially less sensitive to upstream fillets than to chamfers. This is in line with the results obtained for the mean flow. This lower sensitivity of the mean flow to fillets explains the lower sensitivity of the acoustic response.

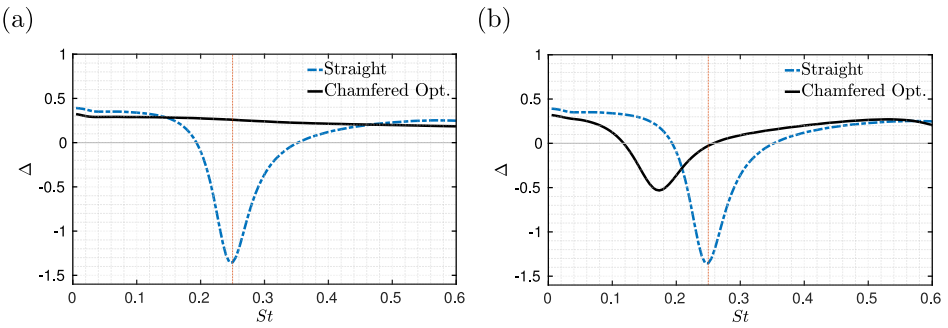

Fig. 9. Absorption coefficient of the straight and optimised holes at different frequencies. (a) Unconstrained problem, i.e $\delta_u^{\max} = L_h$, and (b) $\delta_u^{\max} = 0.1L_h$.

As for downstream modifications, fillets are found to induce larger variations of the acoustic absorption coefficient: the magnitude of the peak is increased from $\Delta = -1.35$ to $\Delta = -1.75$ and $\Delta = -2.0$ for chamfers and fillets, respectively.

5. Optimisation of the acoustic response

In this section, we seek to determine the geometry of the corners of the hole that maximises its acoustic absorption. As seen in Section 4.2, for the same characteristic length, i.e. δ_u, chamfered upstream corners have more prominent effect on the hole's acoustic absorption than any other modifications considered in this paper. Therefore, we optimise the size of upstream chamfers (with a constant angle of 45°). We target to maximise the absorption coefficient, Δ, at a given frequency — in this case the frequency of maximum energy generation for the straight hole, i.e. $St = 0.25$.

The optimisation framework is the same introduced by [28] – but extended to turbulent flows – and relies on a Bayesian optimisation algorithm [60] which is gradient-free and, thus, straightforward to integrate with existing numerical solvers. Formally, the optimisation problem is written as:

$$\arg \max_{\delta_u} \Delta(\delta_u), \tag{13}$$

subject to $\delta_u \in [0, \delta_u^{\max}]$, where $\delta_u^{\max}$ is a parameter selected by the user to constrain the largest possible value of the chamfer. Here, we consider two values of this parameter: $\delta_u^{\max} = 0.1L_h$ and $\delta_u^{\max} = L_h$ for constrained and non-constrained optimisation, respectively.

The optimisation algorithm is implemented in the open-source library `scikit-optimize` (see https://scikit-optimize.github.io/stable/) and is based on Bayesian optimisation using Gaussian processes [60]. In Bayesian optimisation, the objective function (here the absorption coefficient) needs to be evaluated for given inputs (the size of the chamfer). This process is known as sampling. Our numerical approach requires to perform the following four steps for each sampling point: first, a mesh is generated for a given input (δ_u); second, a mean flow is computed solving the RANS equations; third, the acoustic field is obtained by solving the LNSE and; fourth, the value of the absorption coefficient is determined. The optimisation algorithm works as follows. First, the algorithm is initialised by sampling the objective function a prescribed number of times. Then, a Gaussian process which describes the objective function is obtained by fitting it to the initial samples. Based on this Gaussian process, an acquisition function is defined and the next sample point is determined by minimising it. The next sample is computed, the Gaussian process is updated and the acquisition function is minimised again to determine the next sampling point. This process continues until the solution is converged or a prescribed number of iterations is reached.

The parameters used for the optimisation are the following: the Gaussian process estimator is a Matern kernel, the acquisition function is set to `"gp_hedge"`, and the acquisition optimiser is set to `"lbfgs"`. In our implementation, we assume that the objective function is exact (i.e. zero variance) for each sampling point. The algorithm is initialised using five equally-distributed initial points laying at $0 \leq \delta_u \leq \delta_u^{\max}$. The convergence criteria here is defined as $|\delta_u^n - \delta_u^{n-1}| \leq 0.005$, where n is the current step.

First, we consider the non-constrained problem, i.e $\delta_u^{\max} = L_h$. Convergence is reached after 20 iterations and the optimum value of δ_u is found to be equal to the length of the hole L_h. The absorption coefficient of the optimised hole is found to be $\Delta = 0.26$ when optimising for $St = 0.25$. Compared to the straight hole which generates the maximum acoustic energy at this frequency, the optimised hole absorbs acoustic energy. Fig. 9(a) compares the absorption coefficient of the optimised to the straight holes. It can be seen that the optimised hole absorbs acoustic energy over the frequency spectrum of $0 \leq St \leq 0.6$. A linear relationship between the absorption coefficient, Δ, and the frequency, St, is observed with Δ decreasing as St increases.

Fig. 10(a) depicts the mean flow for the optimised hole. It is observed that, for the optimised hole, the separation bubble is fully eliminated and the shear layer remains attached along the hole length up to the downstream corner. This increases the discharge coefficient of the optimised hole to $C_d = 0.7086$ compared to 0.65 for the straight hole.

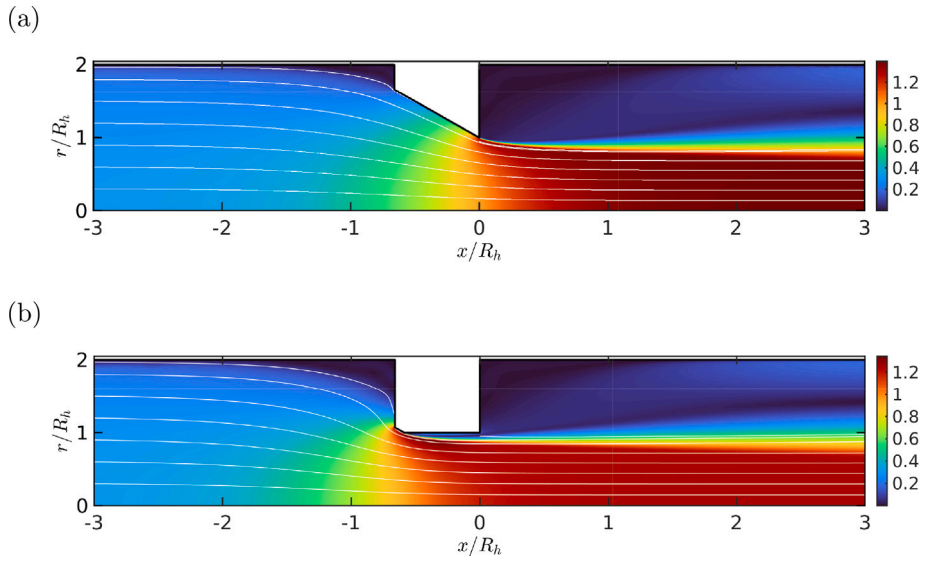

Fig. 10. Mean flow velocity magnitude, $|\bar{\mathbf{u}}|/\bar{u}_h$, obtained for the optimised upstream chamfer. (a) Unconstrained problem, i.e $\delta_u^{\max} = L_h$, and (b) $\delta_u^{\max} = 0.1L_h$.

This optimal geometry obtained can be compared to the results obtained in [28] for a slightly longer hole ($L_h/R_h = 1.0$) with laminar bias flow. While the optimal configuration here is obtained for a large upstream chamfer that suppresses the recirculation zone inside the hole, [28] found that the optimal geometry was a large downstream chamfer. In both cases, the flow–acoustic interaction inside the holes is suppressed in the optimal configurations, which behave acoustically as very thin holes.

We now turn our attention to the constrained problem, i.e. $\delta_u^{\max} = 0.1L_h$, where the upstream chamfer is intentionally restricted to be small. The objective is to determine whether the sensitivity of the acoustic response of the perforations can be exploited to achieve significant improvements through only minor modifications. The optimal chamfer is found to be $\delta_u = 0.072L_h$ and the acoustic absorption $\Delta = -0.02$, which indicates that whistling at that frequency is nearly suppressed. Figs. 9(b) and 10(b) depict the acoustic absorption coefficient and the mean flow, respectively, for the optimal configuration. It is observed that, in this case, the peak of maximum acoustic energy generation is not completely suppressed but instead is moved to frequencies far from the target frequency.

To conclude this section, we analyse the results obtained in this paper in light of the physical interpretation of the phenomenon. When an incoming acoustic wave interacts with the perforation, vorticity is shed from the leading edge, i.e. acoustic energy is transformed into vortical energy. This vorticity is convected by the mean flow along the hole as a convective wave confined to a thin layer (see Fig. 11). If the acoustic forcing is harmonic, the vorticity wavelength is $\lambda_{\text{hyd}} = \frac{u_c}{f}$, where u_c denotes the convection velocity. Vorticity produces sound as it is convected downstream through the perforation; however, the generated sound remains weak and only becomes stronger close to the downstream edge, where the acoustic field is more receptive to acoustic sources due to the sharp edge. When the sound generated close to the downstream edge surpasses the acoustic energy damped at the leading edge, a net generation of acoustic energy occurs (whistling).

Because sound is generated mainly by the vorticity passing close to the downstream edge, the relative phase between the vorticity at the upstream and downstream edges plays a crucial role in the acoustic response. For frequencies where half a wavelength or its multiples fit within the perforation length, the relative sign between the vorticity at the upstream and downstream edges changes. This results in local minima or maxima in the resistance. These are known as hydrodynamic modes [61] and are located approximately at

$$St_{\text{hyd}} = \frac{n}{4C_d}, \tag{14}$$

with $n = 1, 2, 3, \ldots$.

Fig. 6 shows that the first hydrodynamic mode is located at $St = 0.28$ for the straight hole. This mode corresponds to the frequency with the largest acoustic energy generation. In the presence of upstream chamfers, the discharge coefficient increases and the frequency of the first mode decreases, as shown in Eq. (14).

Fig. 11 shows the perturbation vorticity for several configurations of interest. It can be seen that for the unconstrained optimal chamfer edge, vorticity is shed from the downstream edge and, therefore, the acoustic energy generated by vorticity when passing close to the downstream edge is suppressed and, consequently, whistling is eliminated. Additionally, it is observed that while the upstream chamfer modifies the vorticity distribution to a large extend when compared to a straight hole, this remains virtually unmodified for its downstream counterpart. This observation directly relates to the stronger sensitivities obtained for upstream chamfers.

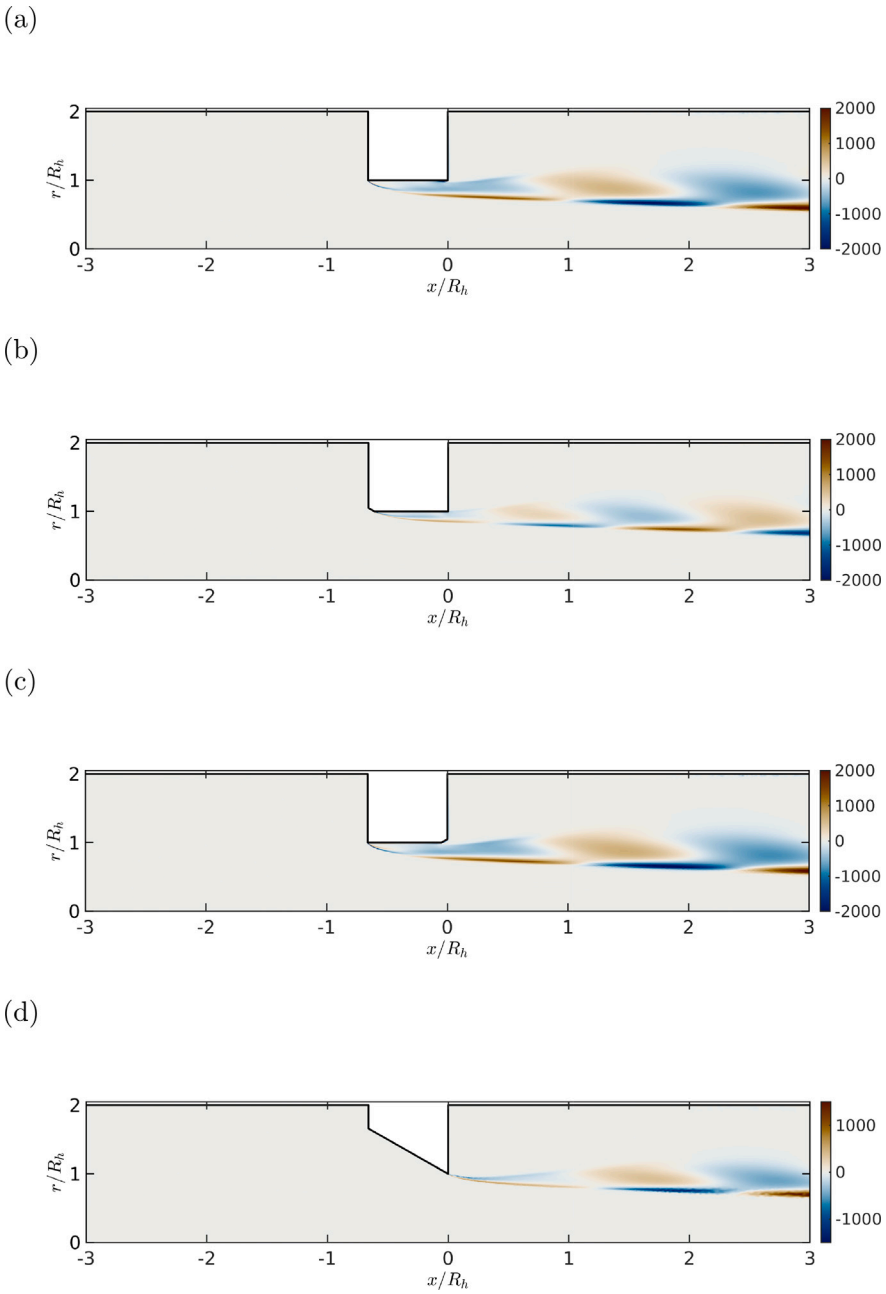

Fig. 11. Real part of normalised perturbation vorticity at $St = 0.25$ obtained for: (a) a straight hole, holes with 45° chamfers of size $\delta/R_h = 5\%$ at the (b) upstream and (c) downstream edges, and (d) hole with optimal upstream chamfer.

6. Conclusion

In this work, we studied numerically the sensitivity of the acoustic response of short circular holes with bias flows to modifications of their upstream and downstream edges. The numerical approach was based on a linearisation of the Navier–Stokes equations (LNSE) about a steady, turbulent mean flow. The linearised equations were solved efficiently in the frequency domain and a

frozen eddy viscosity approach was used to model the turbulence. The numerical results for a straight hole were compared with experimental measurements showing an excellent agreement.

The numerical approach was then used to simulate holes with 45° chamfered edges and circular fillets. Four cases were considered: holes with upstream chamfer and fillet (sharp downstream) and downstream chamfer and fillet (sharp upstream). It was found that the acoustic response and, consequently, the energy absorbed by the holes, was strongly affected by the upstream modifications. In contrast, downstream modifications only mildly affected the acoustic response of the holes. When chamfers and fillets were compared, the acoustic absorption was significantly more sensitive for the former when the modifications are upstream and for the latter when downstream.

The results presented here confirm that the acoustic response of short circular holes with bias flow is strongly sensitive to edge modifications as proposed by Guzman-Inigo et al. [22] using a semi-analytical model. This highlights the need to account for this sensitivity when modelling/manufacturing/designing acoustic systems containing them. In fact, the sensitivity can be exploited to create bespoke geometrical designs of perforations in liners to maximise their energy absorption. Here, we proposed a methodology to achieve this for holes with turbulent flows by extending the methodology proposed by [28] for laminar ones. The results showed that a hole can be optimised to go from one generating 134% more acoustic energy than incident upon it at a given frequency to one that damps 25% of this acoustic energy at that same frequency.

CRediT authorship contribution statement

Juan Guzmán-Iñigo: Writing – review & editing, Writing – original draft, Visualization, Validation, Software, Methodology, Investigation, Formal analysis, Conceptualization. **Dania Ahmed:** Writing – review & editing, Visualization, Software, Investigation. **Aimee S. Morgans:** Writing – review & editing, Supervision, Resources, Project administration, Funding acquisition.

Declaration of competing interest

The authors declare that they have no known competing financial interests or personal relationships that could have appeared to influence the work reported in this paper.

Acknowledgements

The authors acknowledge the European Research Council (ERC) Consolidator Grant AFIRMATIVE (2018–2023).

Appendix. Mesh-independence study

In this section, we present a mesh independence study for the straight hole considered in Section 3. The mean flow is computed using the same mesh and the results are interpolated onto three acoustic meshes comprising 41,450 (coarse), 202,386 (medium) and 809,544 (fine) triangles. Second-order polynomials are used for the three computations. Fig. A.12 shows the acoustic absorption obtained for the three meshes. For the coarse mesh, we observe that the results are unconverged (in mesh size) close to the frequency of strongest generation of acoustic energy. In contrast, the medium and fine meshes are converged across the whole frequency range investigated. In this work, we use the medium mesh as the reference mesh.

Data availability

Data will be made available on request.

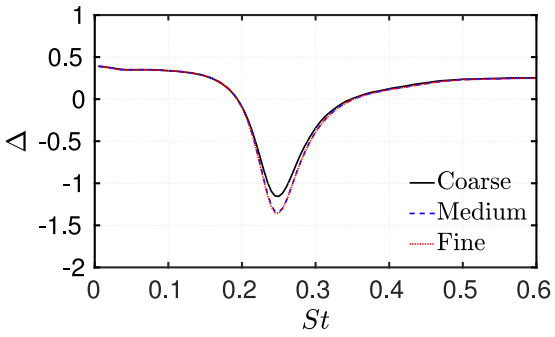

Fig. A.12. Mesh-independence study.

References

[1] S. Gröning, J.S. Hardi, D. Suslov, M. Oschwald, Injector-driven combustion instabilities in a hydrogen/oxygen rocket combustor, J. Propul. Power 32 (3) (2016) 560–573, http://dx.doi.org/10.2514/1.B35768.

[2] W. Armbruster, J.S. Hardi, D. Suslov, M. Oschwald, Injector-driven flame dynamics in a high-pressure multi-element oxygen–hydrogen rocket thrust chamber, J. Propul. Power 35 (3) (2019) 632–644, http://dx.doi.org/10.2514/1.B37406.

[3] P. Brokof, J. Guzmán-Iñigo, A.S. Morgans, M. Son, W. Armbruster, J.S. Hardi, Injection-coupling instabilities in the BKD combustor: Acoustic analysis of the isolated injectors, AIAA J. 61 (6) (2023) 2581–2590, http://dx.doi.org/10.2514/1.J062507.

[4] J. Rupp, J.F. Carrotte, M. M., The use of perforated damping liners in aero gas turbine combustion systems, J. Eng. Gas Turb. Power 134 (7) (2012) 071502, http://dx.doi.org/10.1115/1.4005972.

[5] D. Zhao, X.Y. Li, A review of acoustic dampers applied to combustion chambers in aerospace industry, Prog. Aerosp. Sci. 74 (2015) 114–130, http://dx.doi.org/10.1016/j.paerosci.2014.12.003.

[6] C. Lahiri, F. Bake, A review of bias flow liners for acoustic damping in gas turbine combustors, J. Sound Vib. 400 (2017) 564–605, http://dx.doi.org/10.1016/j.jsv.2017.04.005.

[7] V. Bellucci, P. Flohr, C.O. Paschereit, F. Magni, On the use of Helmholtz resonators for damping acoustic pulsations in industrial gas turbines, J. Eng. Gas Turb. Power 126 (2) (2004) 271–275, http://dx.doi.org/10.1115/1.1473152.

[8] I.D.J. Dupére, A.P. Dowling, The use of Helmholtz resonators in a practical combustor, J. Eng. Gas Turb. Power 127 (2) (2005) 268–275, http://dx.doi.org/10.1115/1.1806838.

[9] P. Brokof, J. Guzmán-Iñigo, D. Yang, A.S. Morgans, The acoustics of short circular holes with reattached bias flow, J. Sound Vib. 546 (2023) 117435, http://dx.doi.org/10.1016/j.jsv.2022.117435.

[10] P. Testud, Y. Aurégan, P. Moussou, A. Hirschberg, The whistling potentiality of an orifice in a confined flow using an energetic criterion, J. Sound Vib. 325 (4) (2009) 769–780, http://dx.doi.org/10.1016/j.jsv.2009.03.046.

[11] X. Jing, X. Sun, Experimental investigations of perforated liners with bias flow, J. Acoust. Soc. Am. 106 (5) (1999) 2436–2441, http://dx.doi.org/10.1121/1.428128.

[12] V. Bellucci, P. Flohr, C.O. Paschereit, Numerical and experimental study of acoustic damping generated by perforated screens, AIAA J. 42 (8) (2004) 1543–1549, http://dx.doi.org/10.2514/1.9841.

[13] M.S. Howe, Attenuation of sound in a low Mach number nozzle flow, J. Fluid Mech. 91 (02) (1979) 209–229, http://dx.doi.org/10.1017/S0022112079000124.

[14] A. Dowling, I. Hughes, Sound absorption by a screen with a regular array of slits, J. Sound. Vib. 156 (3) (1992) 387–405, http://dx.doi.org/10.1016/0022-460X(92)90735-G.

[15] D. Yang, A.S. Morgans, A semi-analytical model for the acoustic impedance of finite length circular holes with mean flow, J. Sound Vib. 384 (2016) 294–311, http://dx.doi.org/10.1016/j.jsv.2016.08.006.

[16] D. Yang, A.S. Morgans, The acoustics of short circular holes opening to confined and unconfined spaces, J. Sound Vib. 393 (2017) 41–61, http://dx.doi.org/10.1016/j.jsv.2016.12.027.

[17] S. Mendez, J.D. Eldredge, Acoustic modeling of perforated plates with bias flow for large-eddy simulations, J. Comput. Phys. 228 (13) (2009) 4757–4772, http://dx.doi.org/10.1016/j.jcp.2009.03.026.

[18] R. Lacombe, S. Föller, G. Jasor, W. Polifke, Y. Aurégan, P. Moussou, Identification of aero-acoustic scattering matrices from large eddy simulation: Application to whistling orifices in duct, J. Sound Vib. 332 (20) (2013) 5059–5067, http://dx.doi.org/10.1016/j.jsv.2013.04.036.

[19] A. Kierkegaard, S. Allam, G. Efraimsson, M. Åbom, Simulations of whistling and the whistling potentiality of an in-duct orifice with linear aeroacoustics, J. Sound Vib. 331 (5) (2012) 1084–1096, http://dx.doi.org/10.1016/j.jsv.2011.10.028.

[20] J. Su, J. Rupp, A. Garmory, J.F. Carrotte, Measurements and computational fluid dynamics predictions of the acoustic impedance of orifices, J. Sound Vib. 352 (2015) 174–191, http://dx.doi.org/10.1016/j.jsv.2015.05.009.

[21] Z. Chen, Z. Ji, H. Huang, Acoustic impedance of perforated plates in the presence of bias flow, J. Sound Vib. 446 (2019) 159–175, http://dx.doi.org/10.1016/j.jsv.2019.01.031.

[22] J. Guzmán-Iñigo, D. Yang, H.G. Johnson, A.S. Morgans, Sensitivity of the acoustics of short circular holes with bias flow to inlet edge geometries, AIAA J. 57 (11) (2019) 4835–4844, http://dx.doi.org/10.2514/1.J057996.

[23] A. Lichtarowicz, R.K. Duggins, E. Markland, Discharge coefficients for incompressible non-cavitating flow through long orifices, J. Mech. Eng. Sci. 7 (2) (1965) 210–219, http://dx.doi.org/10.1243/JMES_JOUR_1965_007_029_02.

[24] P.R. Bullen, D.J. Cheeseman, L.A. Hussain, The effects of inlet sharpness on the pipe contraction pressure loss coefficient, Int. J. Heat Fluid Fl. 9 (4) (1988) 431–433, http://dx.doi.org/10.1016/0142-727X(88)90012-4.

[25] I.E. Idelchik, Handbook of hydraulic resistance, fourth ed., Begell House, 2007, ISBN: 9781567002515.

[26] J. Gikadi, S. Föller, T. Sattelmayer, Impact of turbulence on the prediction of linear aeroacoustic interactions: Acoustic response of a turbulent shear layer, J. Sound Vib. 333 (24) (2014) 6548–6559, http://dx.doi.org/10.1016/j.jsv.2014.06.033.

[27] A. Holmberg, A. Kierkegaard, C. Weng, A frequency domain linearized Navier–Stokes method including acoustic damping by eddy viscosity using RANS, J. Sound Vib. 346 (2015) 229–247, http://dx.doi.org/10.1016/j.jsv.2015.02.030.

[28] J. Guzmán-Iñigo, A.S. Morgans, Designing the edges of holes (with bias flow) to maximise acoustic damping, J. Sound Vib. 575 (2024) 118224, http://dx.doi.org/10.1016/j.jsv.2023.118224.

[29] S. Schmidt, E. Wadbro, M. Berggren, Large-scale three-dimensional acoustic horn optimization, SIAM J. Sci. Comput. 38 (6) (2016) B917–B940, http://dx.doi.org/10.1137/15M1021131.

[30] F. Caeiro, C. Sovardi, K. Förner, W. Polifke, Shape optimization of a Helmholtz resonator using an adjoint method, Int. J. Spray Comb. 9 (4) (2017) 394–408, http://dx.doi.org/10.1177/1756827717703576.

[31] P.V. Kungurtsev, M.P. Juniper, Adjoint-based shape optimization of the microchannels in an inkjet printhead, J. Fluid Mech. 871 (2019) 113–138, http://dx.doi.org/10.1017/jfm.2019.271.

[32] G. Tissot, R. Billard, G. Gabard, Optimal cavity shape design for acoustic liners using Helmholtz equation with visco-thermal losses, J. Comput. Phys. 402 (2020) 109048, http://dx.doi.org/10.1016/j.jcp.2019.109048.

[33] Y. Noguchi, T. Yamada, Level set-based shape optimization of deformable structures for achieving desired sound transmission and reflective responses, Comput. Method Appl. M. 414 (2023) 116190, http://dx.doi.org/10.1016/j.cma.2022.114863.

[34] M. Temiz, Passive noise control by means of micro-perforated plates : developing tools for an optimal design (Ph.D. thesis), Technische Universiteit Eindhoven, 2017.

[35] K. Förner, M.A. Temiz, W. Polifke, I. Lopez Arteaga, A. Hirschberg, On the non-linear influence of the edge geometry on vortex shedding in Helmholtz resonators, in: Proceedings of the 22nd International Conference on Sound and Vibration, 2015.

[36] C. Ji, D. Zhao, Two-dimensional lattice Boltzmann investigation of sound absorption of perforated orifices with different geometric shapes, Aerosp. Sci. Technol. 39 (2014) 40–47, http://dx.doi.org/10.1016/j.ast.2014.08.010.

[37] C. Ji, D. Zhao, N. Han, J. Li, Parametric measurements of the effect of in-duct orifice edge shape on its noise damping performance, J. Sound Vib. 384 (2016) 130–145, http://dx.doi.org/10.1016/j.jsv.2016.08.007.
[38] D. Zhao, C. Ji, B. Wang, Geometric shapes effect of in-duct perforated orifices on aeroacoustics damping performances at low Helmholtz and Strouhal number, J. Acoust. Soc. Am. 145 (4) (2019) 2126–2137, http://dx.doi.org/10.1121/1.5096642.
[39] W.C. Reynolds, A.K.M.F. Hussain, The mechanics of an organized wave in turbulent shear flow. Part 3. Theoretical models and comparisons with experiments, J. Fluid Mech. 54 (2) (1972) 263–288, http://dx.doi.org/10.1017/S0022112072000679.
[40] H.G. Weller, G. Tabor, H. Jasak, C. Fureby, A tensorial approach to computational continuum mechanics using object-oriented techniques, Comput. Phys. 12 (6) (1998) 620–631, http://dx.doi.org/10.1063/1.168744.
[41] F.R. Menter, M. Kuntz, R. Langtry, Ten years of industrial experience with the SST turbulence model, Turbul. Heat Mass Transf. 4 (1) (2003) 625–632.
[42] A. Kierkegaard, S. Boij, G. Efraimsson, A frequency domain linearized Navier–Stokes equations approach to acoustic propagation in flow ducts with sharp edges, J. Acoust. Soc. Am. 127 (2) (2010) 710–719, http://dx.doi.org/10.1121/1.3273899.
[43] A. Kierkegaard, S. Boij, G. Efraimsson, Simulations of the scattering of sound waves at a sudden area expansion, J. Sound Vib. 331 (5) (2011) 1068–1083, http://dx.doi.org/10.1016/j.jsv.2011.09.011.
[44] J. Gikadi, M. Schulze, J. Schwing, S. Foeller, T. Sattelmayer, Linearized Navier-Stokes and Euler equations for the determination of the acoustic scattering behaviour of an area expansion, in: 18th AIAA/CEAS Aeroacoustics Conference (33rd AIAA Aeroacoustics Conference), Colorado Springs, CO, 2012, p. 2292, http://dx.doi.org/10.2514/6.2012-2292.
[45] J. Donea, A. Huerta, Finite Element Methods for Flow Problems, John Wiley & Sons, 2003, http://dx.doi.org/10.1002/0470013826.
[46] M.S.A. s, J. Blechta, J. Hake, A. Johansson, B. Kehlet, A. Logg, C. Richardson, J. Ring, M.E. Rognes, G.N. Wells, The FEniCS Project Version 1.5, Arch. Numer. Softw. 3 (100) (2015) http://dx.doi.org/10.11588/ans.2015.100.20553.
[47] A. Logg, K.A. Mardal, G.N. Wells, et al., Automated solution of differential equations by the finite element method, Springer, ISBN: 978-3-642-23098-1, 2012, http://dx.doi.org/10.1007/978-3-642-23099-8.
[48] P.R. Amestoy, I.S. Duff, J. Koster, J.-Y. L'Excellent, A fully asynchronous multifrontal solver using distributed dynamic scheduling, SIAM J. Matrix Anal. Appl. 23 (1) (2001) 15–41, http://dx.doi.org/10.1137/S0895479899358194.
[49] P.R. Amestoy, A. Guermouche, J.-Y. L'Excellent, S. Pralet, Hybrid scheduling for the parallel solution of linear systems, Parallel Comput. 32 (2) (2006) 136–156, http://dx.doi.org/10.1016/j.parco.2005.07.004.
[50] J. Guzmán-Iñigo, D. Yang, R. Gaudron, A.S. Morgans, On the scattering of entropy waves at sudden area expansions, J. Sound Vib. 540 (2022) 117261, http://dx.doi.org/10.1016/j.jsv.2022.117261.
[51] T.J. Poinsot, S. Lele, Boundary conditions for direct simulations of compressible viscous flows, J. Comput. Phys. 101 (1) (1992) 104–129, http://dx.doi.org/10.1016/0021-9991(92)90046-2.
[52] A.F. Seybert, D.F. Ross, Experimental determination of acoustic properties using a two-microphone random-excitation technique, J. Acoust. Soc. Am. 61 (5) (1977) 1362–1370, http://dx.doi.org/10.1121/1.381403.
[53] T. Poinsot, C. Le Chatelier, S.M. Candel, E. Esposito, Experimental determination of the reflection coefficient of a premixed flame in a duct, J. Sound Vib. 107 (2) (1986) 265–278, http://dx.doi.org/10.1016/0022-460X(86)90237-3.
[54] M. Åbom, Measurement of the scattering-matrix of acoustical two-ports, Mech. Syst. Signal Pr. 5 (2) (1991) 89–104, http://dx.doi.org/10.1016/0888-3270(91)90017-Y.
[55] R. Gaudron, D. Yang, A. Morgans, Acoustic energy balance during the onset, growth, and saturation of thermoacoustic instabilities, J. Eng. Gas Turb. Power 143 (4) (2021) 041026, http://dx.doi.org/10.1115/1.4049347.
[56] S. Boij, B. Nilsson, Scattering and absorption of sound at flow duct expansions, J. Sound Vib. 289 (3) (2006) 577–594, http://dx.doi.org/10.1016/j.jsv.2005.02.017.
[57] I. Dupére, A. Dowling, Absorption of sound near abrupt area expansions, AIAA J. 38 (2) (2000) 193–202, http://dx.doi.org/10.2514/2.952.
[58] M.K. Myers, Transport of energy by disturbances in arbitrary steady flows, J. Fluid Mech. 226 (1991) 383–400, http://dx.doi.org/10.1017/S0022112091002434.
[59] A. Kierkegaard, S. Boij, G. Efraimsson, Simulations of the scattering of sound waves at a sudden area expansion, J. Sound Vib. 331 (5) (2012) 1068–1083, http://dx.doi.org/10.1016/j.jsv.2011.09.011.
[60] B. Shahriari, K. Swersky, Z. Wang, R.P. Adams, N. De Freitas, Taking the human out of the loop: A review of Bayesian optimization, Proc. IEEE 104 (1) (2015) 148–175, http://dx.doi.org/10.1109/JPROC.2015.2494218.
[61] L. Hirschberg, J. Guzman-Inigo, A. Aulitto, J. Sierra, D. Fabre, A. Morgans, A. Hirschberg, Linear theory and experiments for laminar bias flow impedance: Orifice shape effect, in: 28th AIAA/CEAS Aeroacoustics 2022 Conference, 2022, p. 2887, http://dx.doi.org/10.2514/6.2022-2887.